RESEARCH ARTICLE

Tri-reforming of methane over Ni/ZrO$_2$ catalyst derived from Zr-MOF for the production of synthesis gas

Akansha Pandey[1] · Prakash Biswas[1]

Abstract

The increasing concentration of CO$_2$ and CH$_4$ in the environment is a global concern. Tri-reforming of methane (TRM) is a promising route for the conversion of these two greenhouse gases to more valuable synthesis gas with an H$_2$/CO ratio of 1.5–2. In this study, a series of Zr-MOF synthesized via the solvothermal method and impregnation technique was used to synthesize the nickel impregnated on MOF-derived ZrO$_2$ catalyst. The catalyst was characterized by various methods, including N$_2$-porosimetry, X-ray diffraction (XRD), temperature programmed reduction (TPR), CO$_2$-temperature programmed desorption (CO$_2$-TPD), thermo-gravimetric analysis (TGA), chemisorption, field-emission scanning electron microscopy (FE-SEM), and high-resolution transmission electron microscopy (HR-TEM). Characterization results confirmed the formation of the Zr-MOF and nickel metal dispersed on MOF-derived ZrO$_2$. Further, the tri-reforming activity of the catalyst developed was evaluated in a downflow-packed bed reactor. The various catalysts were screened for TRM activity at different temperatures (600–850 °C). Results demonstrated that TRM was highly favorable over the NZ-1000 catalyst due to its desirable physicochemical properties, including nickel metal surface area (2.3 m^2/g$_{cat}$$^{-1}$), metal dispersion (7.1%), and nickel metal reducibility (45%), respectively. Over the NZ-1000 catalyst, an optimum H$_2$/CO ratio of ~ 1.6–2 was achieved at 750 °C, and it was stable for a longer period of time.

Keywords Zirconia-metal–organic-frameworks · Solvothermal method · Methane reforming · Greenhouse gases · H$_2$/CO ratio

Introduction

CH$_4$ and CO$_2$ are the two main constituents of global warming, and their concentration in the atmosphere is increasing day by day due to the burning of fossil fuels, deforestation, urbanization, and rapid industrialization (Fiaschi and Baldini 2009; Yoo et al. 2015). The current global average concentration of CO$_2$ and CH$_4$ in the atmosphere is ~ 420 ppm and ~ 1930 ppb, respectively, and it also shows a sharp increasing trend in the future (Lan et al. 2024). Therefore, reliable technology is essential for the effective conversion of these two problematic gases into valuable

products. An innovative approach to address this challenge is directly converting CO$_2$ and CH$_4$ into the synthesis gas via tri-reforming of methane (TRM) in the presence of suitable heterogeneous catalysts, reactor, and reaction conditions. Most importantly, the flue gas from the power plant can directly be used as a feed in the TRM process (Song and Pan 2004; Halmann and Steinfeld 2006). In addition, the feed composition of this reaction can easily be tuned for a desired H$_2$/CO ratio for the Fischer–Tropsch process. However, to get the desired H$_2$/CO ratio, the design of a suitable catalyst and the reaction process is very challenging (Schmal et al. 2018).

In 2001, Chunshan Song proposed the TRM process, and since then, many noble (Pt, Ru, Rh) and non-noble metal (Ni, Cu, Zn, and Co) catalysts with different supports (CeO$_2$, ZrO$_2$, Al$_2$O$_3$, MgO, SiC) are tested for this reaction (Pan et al. 2002; García-Vargas et al. 2015; Singha et al. 2016a; Al-Fatesh et al. 2018; Kumar and Pant 2020). Very high CH$_4$ conversion (>80%) was reported in the presence of Pt, and it also hindered the re-oxidation of metal during TRM (Pan et al. 2002; Jiang et al. 2013). Ru metal improved the catalytic activity due to its

---

Responsible Editor: George Z. Kyzas

✉ Prakash Biswas
  prakash.biswas@ch.iitr.ac.in; prakashbiswas@gmail.com

1 Department of Chemical Engineering, Indian Institute of Technology Roorkee, Roorkee 247667, Uttarakhand, India

hydrogen spillover characteristics and showed high resistivity for carbon formation (Kumar et al. 2021). Although noble metal was found to be better for the tri-reforming process, however, the cost and availability of noble metal are the main hurdles for large-scale commercial applications (Jiang et al. 2007). Therefore, several studies focused on the development of non-noble metal-based catalysts. Among the non-noble metal catalysts, nickel catalysts have been explored extensively (Kumar et al. (2019)). However, catalyst deactivation due to coke deposition, metal sintering, and re-oxidation of nickel have been reported as major issues (Sun et al. 2012; Lee et al. 2015). To overcome these problems, various nickel-based catalysts were synthesized by different techniques, and Ni/ZrO_2 demonstrated good activity, stability, and coke resistant (Anchieta et al. 2019; Pham et al. 2021). Song and Pan (2004) tested the Ni/ZrO_2 catalyst synthesized by the wet impregnation method and reported very high CH_4 (90%) and CO_2 (65%) conversion with an H_2/CO ratio of ~1.5 at 850 °C under atmospheric conditions. However, the catalyst surface area was low (7.4 m^2/g), and the reaction temperature was high. In addition to that, the catalyst stability and the coke formation data are not reported. Singha et al. (2016b) also synthesized a very stable Ni/ZrO_2 catalyst using the hydrothermal method. At 800 °C and 1 atm pressure, the obtained CH_4 and CO_2 conversion was 95% and 92%, respectively. The reported H_2/CO ratio was ~2. One of the major drawbacks of this study was the use of toxic chemicals during catalyst synthesis, and the coke deposition rate was not reported. Kumar et al. (2019) observed catalyst deactivation due to coke deposition and sintering with Ni/ZrO_2 catalyst synthesized by precipitation followed by wet impregnation.

It was observed from the literature that the nickel particle size, metal dispersion, morphology, nature of support, and catalyst synthesis techniques played an important role on the activity and selectivity of the product (Alli et al. 2023). Therefore, the synthesis of a catalyst with uniform small particle size (10–40 nm) dispersed on mesoporous support and a metal-support interaction is very important for the TRM activity and H_2/CO ratio (Singha et al. 2016b; Schmal et al. 2018). Modification of the catalyst's physicochemical properties is crucial to overcome these difficulties. Therefore, in this study, a new Ni/ZrO_2 catalyst was synthesized from a zirconia metal-organic framework (Zr-MOF) precursor. MOF-derived catalysts have unique structural and functional characteristics (Bai et al. 2016). The MOF-type catalysts, synthesized using metal ions and bridging organic linkers, have recently become an essential family of porous materials (Li et al. 2019). Its porosity can easily be tuned by changing the ligands, solvent, and metal precursors. The stability of the MOF also depends on the metal-ligand bond interaction. Such interactions are significantly influenced by factors such as oxidation state and ionic radius or charge density of the metal ions (Seetharaj et al. 2019). Zr-MOF has a good ability to adsorb methane and carbon dioxide due to its thermal and chemical stability (Cavka et al. 2008; Bai et al. 2016). Zhao et al. (2018) reported that Zr-MOF attained a well-defined and thermally stable structure after high-temperature calcination, providing extraordinary advantages over traditional porous catalyst materials. A few literatures have also shown that the final MOF structure and the yield are also affected by the various synthesis parameters such as metal precursors, ligand, solvent, and their ratios (Cavka et al. 2008; Ragon et al. 2014; Furukawa et al. 2014).

In this study, Zr-MOF was synthesized by the solvothermal method using $ZrOCl_2.8H_2O$ as a metal precursor. The molar ratio of zirconium, ligand, solvent, and calcination temperature were optimized to get the desired MOF structure and surface area. Further, nickel metal was impregnated on Zr-MOF and calcined at an optimum temperature to get the well-dispersed MOF-derived nickel catalyst with a well-defined pore structure. The catalysts were characterized by various techniques. Furthermore, the TRM activity of the catalysts was evaluated in a packed bed reactor to obtain the desired H_2/CO ratio of 1.5–2 for the production of methanol, dimethyl ether, and higher alkenes via the Fischer-Tropsch process. The catalyst stability and the carbon deposition rate were also evaluated. The catalyst activity and stability data were co-related with the physicochemical characteristics of the synthesized catalyst.

Experimental section

Catalyst preparation

Zr-MOF with different zirconia was synthesized by the solvothermal method described by Cavka et al. (2008). In the typical procedure, required amounts of $ZrOCl_2.8H_2O$ (0.75–6 mmol) supplied by Loba Chemie Pvt. Ltd., India, with 98% purity and 1,4 benzene dicarboxylic acid (BDC, 98%, HiMedia Laboratories Pvt. Ltd., India) (0.75–6 mmol) were dissolved in N, N-dimethylformamide (DMF, 99%, Thomas Baker chemicals Pvt. Ltd., India) (1500 mmol) at room temperature under continuous stirring. The obtained mixture was sealed in a Teflon-lined autoclave and placed in a hot air oven at 120 °C for 24 h to complete the crystallization process. After crystallization, the autoclave was cooled to room temperature, and the resulting white gel solid obtained was filtered in a vacuum filtration unit. After filtration, the wet solid was washed thoroughly several times with DMF for the complete removal of all the impurities. Then, the washed solid was dried in a hot air oven at 100 °C for 12 h. The obtained white crystals were crushed in a mortar and pestle for further testing. Based on the molar ratio of zirconia, organic ligand, and solvent used during the synthesis, the names of the different Zr-MOFs were assigned, as shown in Table 1.

The Zr-MOF synthesized was further calcined at various temperatures (400–800 °C) for 5 h in a muffle furnace.

During the Zr-MOF synthesis, the amount of ZrO_2 precursor and BDC varied from 0.75 to 6 mmol, and the DMF amount was kept constant (1500 mmol). The amount of ZrO_2 precursor and BDC was increased by keeping the ratio constant to verify the crystal growth and structure of MOF and to enhance the production of Zr-MOF in each batch.

A total of 5 wt.% Ni/ZrO_2 catalyst derived from MOF was prepared using the impregnation technique. Initially, the required amount of nickel salt ($Ni(NO_3)_2.6H_2O$, 98%) supplied by Loba Chemie Pvt. Ltd., India, was dissolved in ethanol. Further, the Zr-MOF powder was added slowly to the salt solution and stirred continuously until the paste formed. After that, the paste was dried overnight at 100 °C in a hot air oven and calcined in the presence of air at 700 °C for 5 h in a muffle furnace. After nickel metal impregnation, the resulting catalysts were named NZ-250, NZ-500, NZ-1000, NZ-1500, and NZ-2000, respectively, where "N" represented the 5 wt.% nickel and "Z" represented the different types of Zr-MOF, as shown in Table 1.

Catalyst characterization

The thermal stability of the Zr-MOF was analyzed by performing thermo-gravimetric analysis (TGA) in an EXSTAR TG/DTG 6300 instrument (Japan). The powder Zr-MOF was heated from 35 to 900 °C at a heating rate of 10 °C/min under the flow of air (200 ml.min^{-1}).

The crystal structure of Zr-MOF and Ni/ZrO_2 catalyst derived from MOF was characterized by the X-ray powdered diffraction (XRD) analysis in an Emp3, Malvern Panalytical (Netherlands) instrument equipped with a Ni-filtered Cu-Kα radiation source ($\lambda = 1.5418$ nm). The XRD was performed at a 2θ interval of 5–90° with a sweep of 0.1°/sec and a time constant of 30 s.

The specific surface area of the catalysts was determined by the nitrogen adsorption–desorption method at liquid nitrogen temperature with Autosorb iQ2 (Quantachrome Instruments, USA) equipment. Before each analysis, the catalyst was pretreated under the flow of helium (20 cc. min^{-1}) at 150 °C for 5 h.

The hydrogen temperature-programmed reduction (H_2-TPR) and CO_2 temperature-programmed desorption (CO_2-TPD) were analyzed in a Micrometrics Pulse Chemisorb 2750 instrument (USA). In H_2-TPR analysis, ~ 30–40 mg of sample was degassed at 150 °C for 2 h under the flow of argon (20 cc.min^{-1}) and then cooled to room temperature. For reduction, a mixture gas (10 vol.% H_2 in argon) was passed through the catalyst placed inside the U-shaped quartz tube. The reduction temperature was increased from 30 to 1000 °C at a heating rate of 10 °C/min, and the hydrogen amount present in the effluent was continuously monitored with the help of a thermal conductivity detector (TCD) connected online.

Prior to the CO_2-TPD analysis, the sample was degassed at 150 °C for 2 h under the helium flow of 20 cc/min, followed by purging pure CO_2 for 45 min on the catalyst surface. Additionally, the sample was heated at a rate of 10 °C/min from 30 to 1000 °C, and the desorbed amount of CO_2 was continuously measured with the help of a TCD.

Nickel particle size and metal dispersion were determined by H_2-chemisorption in a Micrometrics Pulse Chemisorb 2750 instrument (USA). Before each analysis, the catalyst was degassed at 150 °C for 2 h under the argon flow of 20 cc.min^{-1}. Further, the catalyst was reduced by pure H_2 at a reduction temperature determined by TPR for 2 h and then cooled to room temperature (30 °C) under a continuous argon flow at 20 cc.min^{-1}. Afterward, the chemisorption experiments were performed by pulse injection of pure hydrogen (99.999%) at an interval of 5 min until the TCD displayed the identical hydrogen peak area.

The surface morphology of the catalysts was examined by field-emission scanning electron microscopy (FE-SEM) with a Carl-Zeiss Ultra-Plus instrument (Germany). Before the analysis of FE-SEM, a gold coating was applied to the powder catalyst using an Edwards S150 sputter coater (USA). To prevent the particle charging, the coating process was carried out in an argon environment. Subsequently, the FE-SEM study was carried out at 20 kV under vacuum.

Transmission electron microscopy (TEM) images of Zr-MOF, reduced Ni/ZrO_2 catalyst derived from MOF and spent catalysts were taken by the JEOL LEM 2100 microscope from Japan, operating at 200 kV accelerated voltage. Prior to the TEM analysis, the sample was prepared following the method used in our earlier research work (Pandey et al. 2024).

Table 1 Catalyst molar composition with abbreviation

ZrO_2 precursor (mmol)	BDC (mmol)	DMF (mmol)	Molar ratio of Zr/BDC/DMF	Abbreviation	Amount of Zr-MOF formed (g)
0.75	0.75	1500	1/1/2000	Z-2000	0.2
1.00	1.00	1500	1/1/1500	Z-1500	0.3
1.50	1.50	1500	1/1/1000	Z-1000	0.5
3.00	3.00	1500	1/1/500	Z-500	0.9
6.00	6.00	1500	1/1/250	Z-250	2.2

The quantity of coke deposition on the utilized catalyst was measured using the carbon-hydrogen–nitrogen-sulfur (CHNS) analyzer (Model-Vario solid sample, Elementar, Germany). In the standard procedure, the temperatures in the reduction and combustion chambers were maintained at 850 °C and 1150 °C, respectively. The sample (~2 mg) was positioned in a tin boat, and the testing was carried out in an oxygen environment.

The Fourier transform infrared (FTIR) spectra were recorded on a Bruker Tensor-II (Germany) spectroscopy from 4000 to 500 cm^{-1} at room temperature. The samples were mixed with potassium bromide, and a pellet was formed for the analysis.

Catalytic activity test

Catalytic activity was examined in an Inconel packed bed downflow reactor (T-045, Amar Equipment Pvt. Ltd., India) setup as shown in Fig. 1.

The reactor was placed inside a tubular furnace (ATS, USA) equipped with a programmable temperature controller. In a typical experiment, the powder catalyst was well mixed with quartz powder and placed in the middle section of the reactor with the help of quartz wool. Prior to each experiment, the catalyst was reduced in situ under the flow (40 cc.min^{-1}) of a mixture gas (50% H_2 in N_2) for 2 h at a temperature obtained in TPR of individual catalysts. After

that, the desired reaction temperature was achieved under continuous nitrogen flushing through the reactor. After achieving the desired reaction temperature, feed gases (CH_4, O_2, CO_2, and N_2) were passed through the preheater maintained at 300 °C. The flow of feed gases was maintained with the help of a mass flow controller (MFC) supplied by Brooks Instruments, USA. The water was fed with the help of an HPLC pump (Teledyne SSI, USA) and passed through a vaporizer maintained at 300 °C. After the reaction, the product effluent was passed through a condenser connected with a Julabo chiller (F20, Germany). The temperature of the chiller was maintained at ~5 °C for complete condensation of the condensable. The obtained liquid and gas products were separated in a gas–liquid separator. The composition of the liquid product was analyzed in the NMR (Spinsolve 80 carbon, Magritek, Germany) to measure the formation of liquid hydrocarbon, if any. However, the gaseous product was analyzed in the online gas chromatography (GC) by Centurion Scientific (model-5800, India) equipped with a molecular sieve column (Ms 13x, 3 m) connected to the TCD and Porapak-Q column (2 m) associated with flame ionization detector (FID). The reactant conversion and product selectivity were calculated using the following Eqs. (1) and (2), respectively. The carbon balance was within the $90 \pm 10\%$ range.

$$(CH_4 \; or \; CO_2) \; conversion \; (\%) = \left[(\text{initial moles of } CH_4 \text{ or } CO_2 - \text{final moles of } CH_4 \text{ or } CO_2)/\text{initial moles of } CH_4 \text{ or } CO_2\right] \times 100\% \quad (1)$$

$$Product \; selectivity \; (\%) = \left[\text{moles of the specific product}/\text{total moles of the products}\right] \times 100\% \quad (2)$$

Fig. 1 Schematic diagram of experimental setup

Results and discussion

Thermal stability of Zr-MOF

The TGA profile of the Zr-MOF is shown in Fig. 2. For all Zr-MOF, three steps of weight loss were detected. In stage (I) (< 110 °C), a slight weight loss was observed due to the removal of adsorbed water, and in the second stage (II) (110–500 °C), weight loss was observed due to the removal of DMF solvent. For all the MOF, the approximate second stage observed weight loss was ~24–31%. At ≥ 500 °C (stage III), major weight loss was observed due to the decomposition of the organic framework and the formation of pure zirconium oxide (Ardila-Suárez et al. 2019; Sai et al. 2020). Liu et al. (2019) also reported a similar TGA pattern for Zr-MOF.

X-ray diffraction (XRD)

The XRD pattern of the Zr-MOF before calcination is shown in Fig. 3. The XRD peaks detected at the 2θ value of 7.3°, 12.1°, 14.2°, 17.1°, and 25.8° represented the (111), (220), (311), (400), and (442) crystal planes of Zr-MOF (Ragon et al. 2014; Sai et al. 2020).

In Fig. 3, from Z-2000 to Z-250, the zirconia content in the sample is increasing. For Z-1000, the observed intensity of all the peaks were comparatively better with respect to other Zr-MOF, and the peak at the 2θ value of 7.3° was more intense, indicated better crystal formation. These XRD patterns suggested that the formation of MOF structure was controlled significantly by the ratio of zirconia precursors to solvent. The low-intensity peaks indicated the hindrance of the formation of the MOF structure due to the use of excess solvent (DMF)
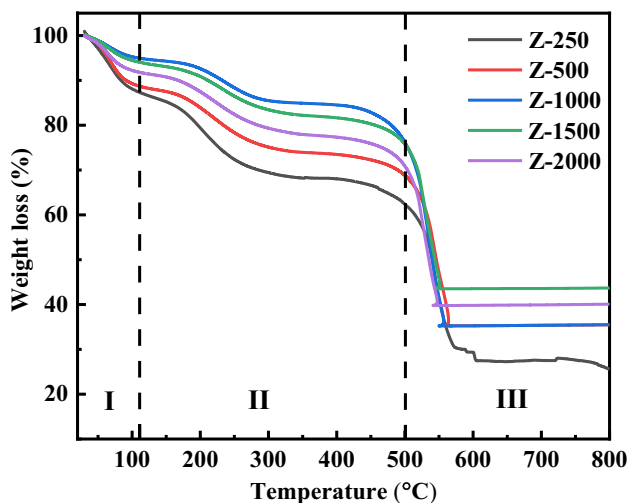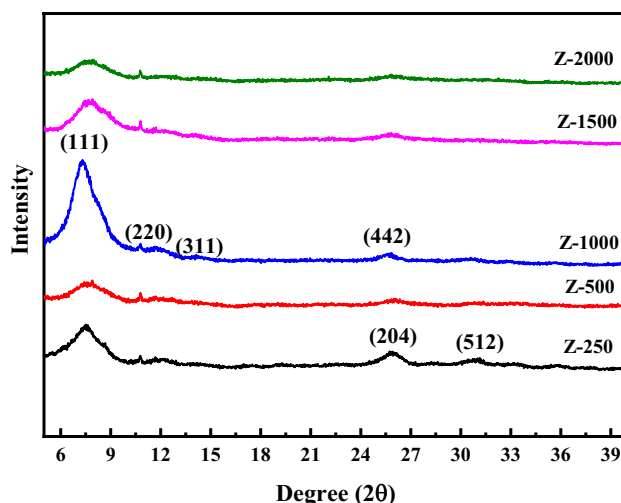
Fig. 3 XRD pattern of Zr-MOF

during the synthesis of Z-2000 and Z-1500, respectively. On the other hand, for Z-500 and Z-250, the intensity of the XRD peaks was also low, indicated the hindrance of MOF formation due to the presence of less solvent (DMF). These results suggested an appropriate ratio of metal precursors to solvent was essential to achieve the desired MOF structure. The solvent acted as a structure/crystal-building agent and controlled the deprotonation of organic carboxylate ligand (BDC) (Seetharaj et al. 2019). Ardila-Suárez et al. (2019) reported a similar observation for the synthesis of Zr-MOF. At a low zirconia precursor ($ZrOCl_2.8H_2O$) to solvent (DMF) ratio, the observed XRD peak intensity was low, which indicated low crystallinity. The XRD pattern represented in Fig. 3 suggested that a better MOF structure was detected for Z-1000 as compared to other Zr-MOFs synthesized.

The effect of calcination temperature (400–800 °C) on the MOF structure of Z-1000 MOF was also studied, and the obtained XRD patterns are illustrated in Fig. 4. The Z-1000 MOF calcined at different temperatures were represented as Cal-X (X = 400, 500, 600, 700, and 800). For Cal-400, an almost similar XRD pattern of MOF was observed, which indicated the stability of the Zr-MOF structure up to 400 °C. This result is also supported by the TGA data (Fig. 2). However, for Cal-500, additional new peaks with very sharp intensity at the 2θ values of 30.2°, 35.2°, 50.8°, and 60.3° were detected corresponding to the (101), (110), (200), and (211) crystal lattice planes of tetragonal phase of ZrO_2 (JCPDS: 01–079-1771, Horti et al. 2020). This result indicated the breakage of MOF structure and the formation of ZrO_2. Further increasing the calcination temperature to 600 °C (Cal-600), the intensity of the peaks (30.2°, 35.3°, 50.8°, and 60.3°) corresponding to the tetragonal ZrO_2 decreased, and simultaneously new peaks at the 2θ values of 24.4°, 28.3°, and 31.6°, related to (011), (− 111), and (200),
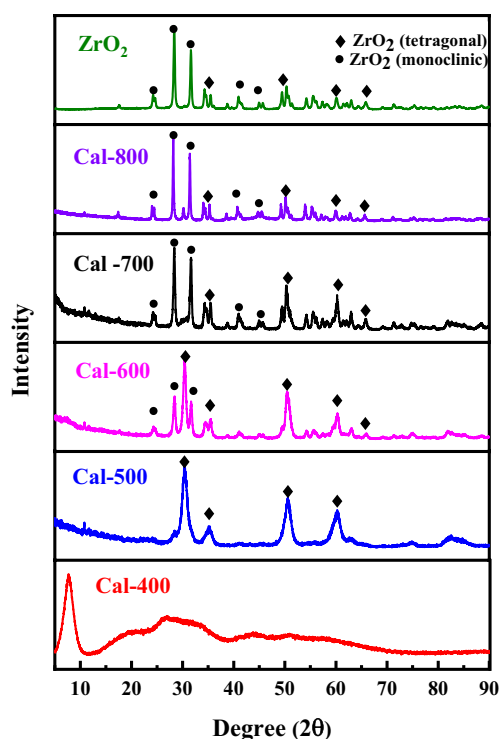
Fig. 2 TGA profile of the Zr-MOF

Fig. 4 XRD pattern of Zr-MOF at various calcination temperatures

Fig. 5 XRD pattern of Ni/ZrO$_2$ catalyst derived from MOF

crystal plane of monoclinic ZrO$_2$ appeared with significant intensity (JCPDS: 37–1484). Beyond 600 °C, a tetragonal to monoclinic phase transformation of ZrO$_2$ was noticed (Finsel et al. 2019; Horti et al. 2020). The XRD patterns of Cal-700 and Cal-800 catalysts indicated a combined tetragonal and monoclinic phase of ZrO$_2$ (Walker et al. 2012), almost similar to the XRD patterns of a commercial ZrO$_2$. These results suggested that the MOF structure of Z-1000 converted to pure ZrO$_2$ beyond the calcination temperature of 700 °C (Tu et al. 2023).

The XRD pattern of reduced Ni/ZrO$_2$ catalyst derived from MOF calcined at 700 °C is shown in Fig. 5. All the catalyst was reduced at a temperature (Fig. 7, Table 2) suggested by the TPR study of the respective catalyst. The peaks corresponding to nickel were detected at the 2θ values of 44.4°, 51.6°, and 76.2°, representing the (111), (200), and (220) lattice planes of the cubic nickel metal (JCPDS: 04–0850, Biswas and Kunzru 2007). However, the peaks at the 2θ values of 28.3°, 31.6°, 35.2°, 50.1°, and 62.7° corresponded to the (− 111), (200), (002), (022), and (113) lattice planes of monoclinic ZrO$_2$ (JCPDS: 37–1484), whereas the diffraction peaks at 2θ values of 30.2°, 35.2°, 50.8°, and 60.3° belong to (101), (110), (200), and (211) lattice planes of the tetragonal ZrO$_2$ (JCPDS: 01–079-1771). It was noticed that after nickel impregnation and reduction, the peaks corresponding to the tetragonal phase of ZrO$_2$ were dominated.
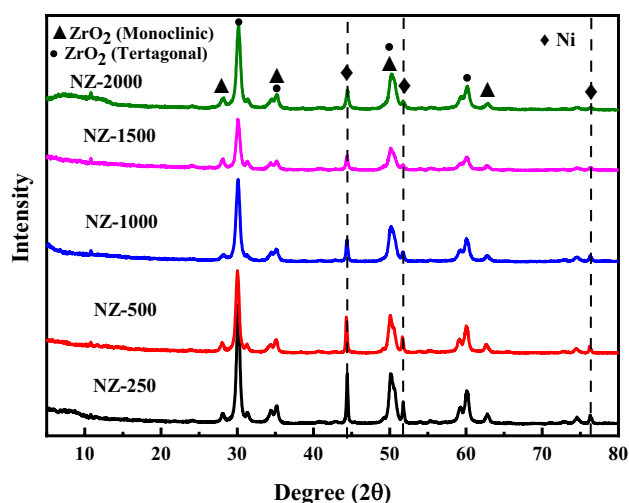
The average nickel crystallite size was determined based on the diffraction peaks detected at the 2θ values of 44.4°, 51.8°, and 76.3°, respectively. The determined nickel crystallite size was in the range of 50.2–73.7 nm (Table 2). The FTIR analysis (Fig. S4) of the catalysts also supported the XRD results.

BET surface area

Figure 6a illustrates the N$_2$-porosimetry of Zr-MOF. The recorded isotherms represented a combination of both type I and type IV isotherms, respectively. Type I isotherm corresponded to the microporous materials with a pore size of up to 2 nm, whereas type IV was related to the mesoporous materials with a pore size of 2–50 nm. According to the recorded isotherms, the adsorption–desorption branches exhibited an H2 hysteresis loop with a wide pore width (Ardila-Suárez et al. 2019). The average BET surface area, pore volume, and pore size of the synthesized MOF are summarized in Table 2. It was observed that Z-250 and Z-500 showed a surface area of ~ 507 m^2/g, whereas the surface area of Z-1000 increased and reached to 635.9 m^2/g. Further, the specific surface area of Z-1500 (437.2 m^2/g) and Z-2000 (414.9 m^2/g) decreased due to the presence of the lower amount of metal precursor and linker in DMF. For all the catalysts, the pore size distribution (PSD) curve obtained supported the formation of both microspores and mesopores (Fig. S1a). The average pore diameter and total pore volume of the Zr-MOF were in the range of 2.3–2.5 nm and 0.233–0.396 cm^3/g, respectively.

Figure 6b shows the isotherms of the Ni/ZrO$_2$ catalysts derived from MOF. For all catalysts, a type IV isotherm was observed after the addition of nickel metal, while

Environmental Science and Pollution Research (2024) 31:35069–35082   35075
Table 2 Physio-chemical characteristics of the catalyst

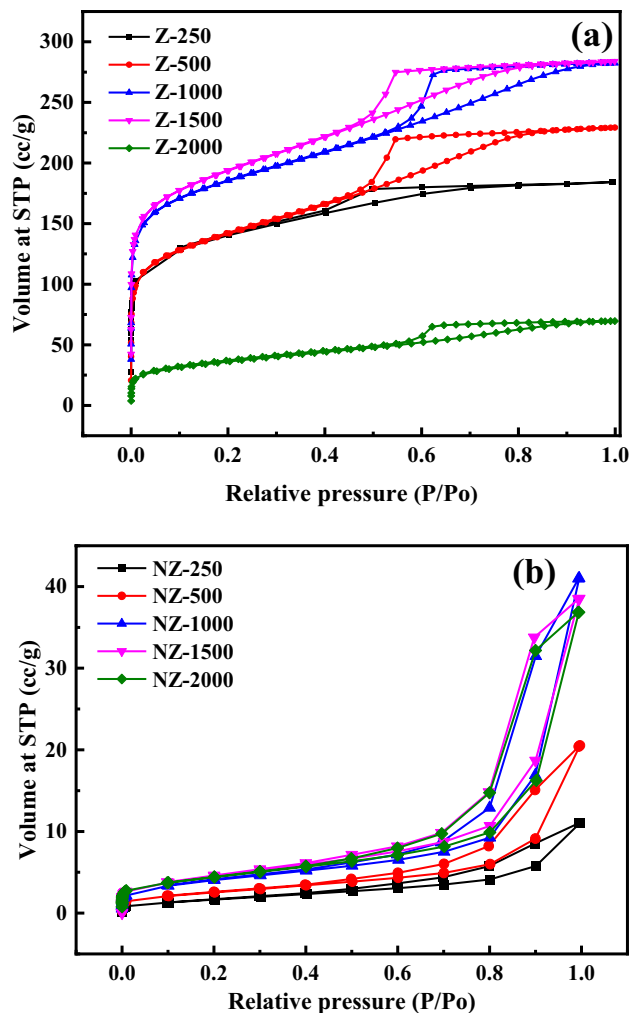| Catalysts	BET surface area (m²·g⁻¹)	Total pore volume (cm³·g⁻¹)	Pore diameter (nm)	Ni crystallite size from XRD (nm)	Reduction temperature (°C)	H₂ consumption (mmol·g_cat⁻¹)	Reducibilty of Ni (%)	Basic strength (mmol·g_cat⁻¹)	Nickel metal dispersion (%)	Ni metal surface area (m²·g_cat⁻¹)
Z-2000	414.9	0.233	2.3	-	-	-	-	0.003	-	-
Z-1500	437.2	0.274	2.5	-	-	-	-	0.003	-	-
Z-1000	635.9	0.396	2.5	-	-	-	-	0.004	-	-
Z-500	507.2	0.335	2.4	-	-	-	-	0.004	-	-
Z-250	507.1	0.285	2.3	-	-	-	-	0.004	-	-
NZ-2000	15.3	0.057	14.9	52.2	447.4	2.18	39.3	0.063	0.8	0.3
NZ-1500	15.6	0.059	15.3	54.8	412.2	2.65	42.2	0.012	1.7	0.6
NZ-1000	16.1	0.063	18.0	50.2	443.1	2.80	45.1	0.018	7.1	2.3
NZ-500	8.8	0.032	14.4	62.2	466.4	2.43	38.7	0.023	1.3	0.4
NZ-250	5.7	0.017	11.9	73.7	417.7	2.01	36.2	0.051	0.7	0.2

Fig. 6 N₂-porosimetry of (**a**) Zr-MOF and (**b**) Ni/ZrO₂ catalysts derived from MOF

the adsorption–desorption branches represented the H3 hysteresis loop. The BET surface area for all the catalysts dropped significantly (5.7–16.1 m²/g) because of the deformation of the MOF structure after calcination at 700 °C (Tu et al. 2023). The highest surface area of 16.1 m²/g was obtained for the NZ-1000 catalyst, and this value was comparable with the values reported for the Ni/ZrO₂ catalyst in the previous literature (Kumar et al. (2019); Pandey et al. 2024). The PSD curve (Fig. S1b) for the Ni/ZrO₂ catalyst derived from MOF represented mesopores structure with wide pore width (2–15 nm). However, for the NZ-1000 catalyst, the pore width was < 5 nm. The average pore diameter and total pore volume of the Ni/ZrO₂ catalysts derived from MOF were in the range of 11.9–18.0 nm and 0.017–0.063 cm³/g, respectively.
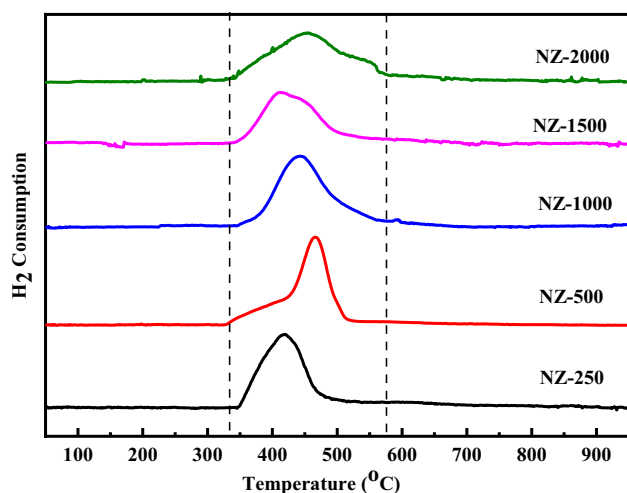
Fig. 7 TPR profile of Ni/ZrO$_2$ catalysts derived from MOF

TPR

The reduction profile of the Ni/ZrO$_2$ catalysts derived from MOF calcined at 700 °C is shown in Fig. 7. For all the catalysts, a wide and broad reduction peak was detected in the temperature range of 340–580 °C due to nickel (Kumar et al. 2023). No reduction peak corresponding to ZrO$_2$ was observed because of its high thermal stability (Biswas and Kunzru 2007). For all the catalysts, the typical nickel reduction temperature peak was in the range of 412–466 °C. This high-temperature reduction indicated strong metal support interaction (Zhen et al. 2015).

The H$_2$ consumption and the reducibility of nickel metal were calculated using the TPR data; the results are summarized in Table 2. The H$_2$ consumption of all catalysts was in the range of 2.01–2.80 mmol. g_{cat}^{-1}, and the reducibility of nickel metal ranged from 36.2 to 45.1%. The maximum hydrogen consumption (2.8 mmol. g_{cat}^{-1}) and the reducibility of nickel metal (45.1%) were obtained for the NZ-1000 catalyst.

TPD (CO$_2$)

The basic strength of the Ni/ZrO$_2$ catalysts derived from MOF was determined by the CO$_2$-TPD analysis. The TPD profile is plotted in Fig. 8, and the basic strength of the catalysts is summarized in Table 2, respectively.

As shown in Table 2, the basic strength of Zr-MOF was low (0.003–0.004 mmol. g_{cat}^{-1}) due to the presence of organic ligand (BDC) and solvent (DMF). However, for the calcined Ni/ZrO$_2$ catalyst derived from MOF, the basic strength increased significantly, and it was in the range of 0.012–0.063 mmol. g_{cat}^{-1}. It was observed that the basic
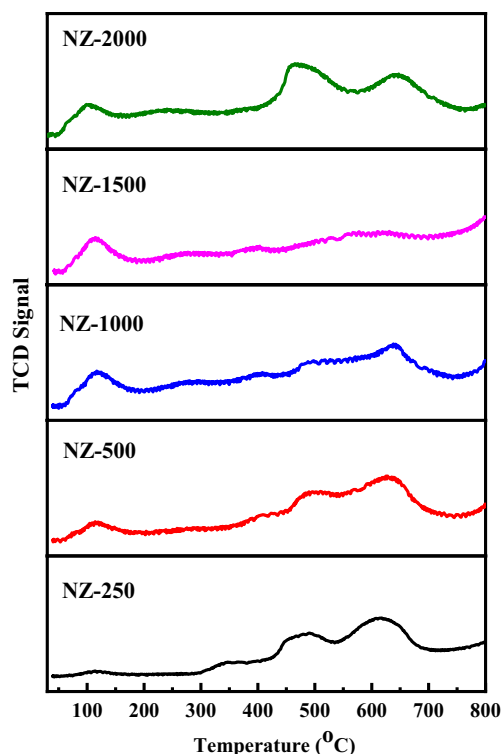

Fig. 8 CO$_2$-TPD profile of Ni/ZrO$_2$ catalysts derived from MOF

strength values passed through minima with increasing the zirconia precursor content (Z-2000 to Z-250) during the catalyst synthesis (Table 2). This result indicated that the zirconia precursors, ligand, and solvent ratio played an important role in controlling the basic strength of the final catalysts. The basic strength in the catalysts was increased due to the removal of BDC and DMF from the MOF structure after calcination at 700 °C, and Zr-MOF was transformed to pure ZrO$_2$ having moderate basic strength (Wang et al. 2021). The maximum strong strength basic sites (400–700 °C) (Fig. 8) were observed for the NZ-2000 catalyst with the value of 0.063 mmol. g_{cat}^{-1}. However, for NZ-1500 (0.012 mmol. g_{cat}^{-1}) and NZ-1000 (0.018 mmol. g_{cat}^{-1}) catalysts, similar CO$_2$-TPD profiles with weak (~ 120 °C) and moderate strength (~ 650 °C) basic sites were detected (Fig. 8).

H$_2$-pulse chemisorption

The H$_2$ pulse chemisorption method was used to determine the nickel metal dispersion and the active nickel metal surface area of the Ni/ZrO$_2$ catalysts derived from MOF. As shown in Table 2, the calculated nickel metal dispersion for all the catalysts was very high (0.7–7.1%). The maximum nickel metal dispersion of 7.1% was obtained for the NZ-1000 catalyst. The calculated nickel metal surface area ranged from 0.2 to 2.3 m^2. g_{cat}^{-1}, and it was also maximum (2.3 m^2. g_{cat}^{-1}) for NZ-1000 catalyst. The highest nickel

metal dispersion and metal surface area for the NZ-1000 catalyst was probably due to its highest surface area, as observed in the BET analysis (Alli et al. 2023).

SEM and HR-TEM

The SEM images of Zr-MOF exhibited a dense morphology (Fig. S2). However, clear morphological changes were observed for the reduced Ni/ZrO_2 catalyst derived from MOF. NZ-2000 and NZ-1500 displayed spherical-shaped particles closely aligned with each other. In contrast, NZ-1000 exhibited well-aligned spherical particles (Wen et al. 2017; Pandey et al. 2024). Furthermore, as the amount of zirconia precursors increased (NZ-500 and NZ-250) during the synthesis, agglomerated clusters and compactness were found to be increased. The BET and PSD analysis also demonstrated the changes in porosity. The FE-SEM results suggested that the morphology of the catalysts was significantly influenced by the molar ratio of the precursor and solvent, as well as by the addition of nickel followed by calcination.

The TEM image of the Zr-MOF after drying (Fig. S3(a)) showed the ill-defined nano-sheets arranged randomly, and selected area electron diffraction (SAED) in Fig. S3(b) illustrated the absence of crystallinity. The calculated average particle size of Zr-MOF was ~185 nm (Fig. S3(c)). Zhao et al. (2018) reported the particle size of UiO-66 in the range of 150–400 nm. For reduced Ni/ZrO_2 catalyst derived from MOF (NZ-1000), very well-dispersed nickel nanoparticles were visible (Fig. S3(d)). The catalyst was crystalline in nature, as shown in the SEAD (Fig. S3(e)). The EDX mapping also confirmed the even dispersion of Ni-metal on the catalyst (Fig. S3(f)). The particle size histogram (Fig. S3(g)) indicated the average nickel particle size was ~32 nm. This value was slightly lower than the nickel crystallite size (~50 nm) calculated from XRD. The difference might be due to the error in the XRD peak area calculated for nickel.

Catalyst activity

Effect of catalysts

Initially, the TRM activity of all the catalysts synthesized was screened at the optimum reaction condition reported in our previous study (Pandey et al. 2024). The result obtained is plotted in Fig. 9a. For all the catalysts, the CH_4 conversion was very high ($\geq 80\%$), and the maximum CH_4 conversion of 96.2% was obtained for the NZ-1000 catalyst. The highest CH_4 conversion over NZ-1000 catalyst was due to its high degree of nickel metal reducibility (45.1%), nickel metal dispersion (7.1%), active surface area (2.3 m^2/g_{cat}^{-1}), and smaller nickel crystallite size of 50.2 nm (Schmal et al. 2018). Similarly, for the
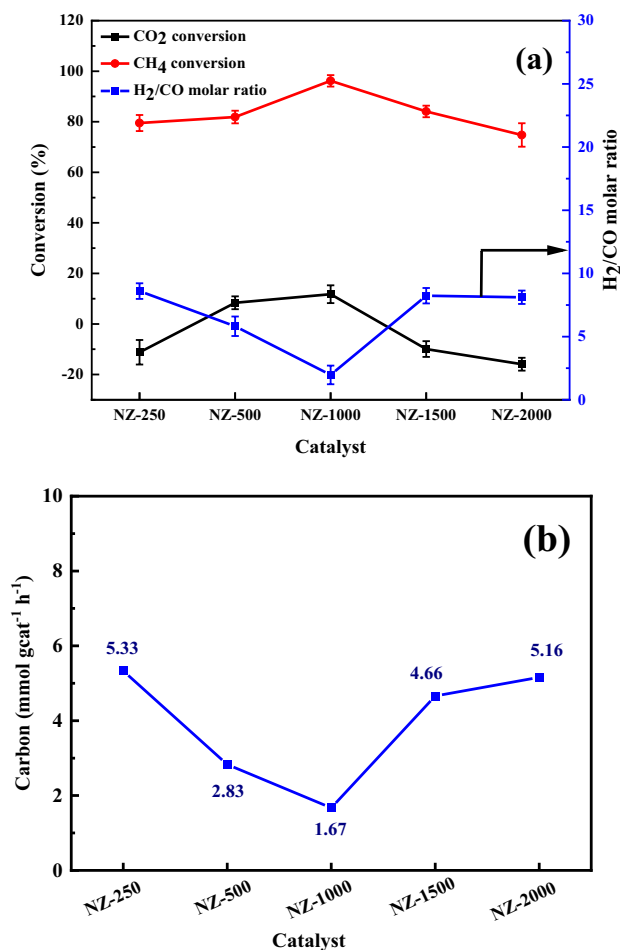

Fig. 9 (**a**) Performance of Ni/ZrO_2 catalysts derived from MOF, (**b**) carbon deposition rate over all the spent catalysts. Reaction condition: Feed ($CH_4/CO_2/O_2/H_2O/N_2$) ratio of (1/0.5/0.1/0.0125/1), 700 °C, 1 atm., and 1 g catalyst

NZ-1000 catalyst, the CO_2 conversion was also maximum (11.8%) because of its moderate basicity and high oxygen mobility of ZrO_2, which activated the adsorption of CO_2 molecules (Wang et al. 2021). In addition to that, the smallest nickel particle size (~32 nm) in NZ-1000 helped to improve the accessibility of ZrO_2 sites for the adsorption of CO_2 molecules (Kumar et al. 2019). However, for NZ-250, NZ-1500, and NZ-2000 catalysts, the observed CO_2 conversion was negative (~11–15%). The negative CO_2 conversion was observed due to the dominance of reverse CO_2 hydrogenation ($CO_2 + 2H_2 \leftrightarrow C + 2H_2O$; $\Delta H°_{298} = -90$ kJ/mol), reverse CO_2 methanation ($CO_2 + 4H_2 \leftrightarrow CH_4 + 2H_2O$; $\Delta H°_{298} = -165$ kJ/mol), and water gas shift reactions (WGSR) ($CO + H_2O \leftrightarrow CO_2 + H_2$; $\Delta H°_{298} = 43$ kJ/mol), respectively, at the operated reaction condition used (Zhang et al. 2014; Chein and Hsu 2018). Solov'ev et al. (2012) also observed a negative CO_2 conversion of 22% at 710 °C in the presence of $Ni-Al_2O_3$

catalyst. This negative CO_2 conversion was observed due to the re-oxidation of metallic nickel and complete oxidation of methane ($CH_4 + 2O_2 \leftrightarrow CO_2 + 2H_2O$) (Song and Pan 2004). Garca-Vargas et al. (2015) also reported negative CO_2 conversion over Ni-Mgβ-SiC catalyst in various reaction conditions. It has been reported that nickel metal re-oxidation during the reaction facilitated the water–gas shift reaction, which again produced CO_2 during the tri-reforming process (Pham Minh et al. 2021).

As shown in Fig. 9a, the observed H_2/CO ratio passed through a minimum with decreasing the zirconia content in the catalyst. Over NZ-1000, the optimum H_2/CO ratio of ∼2 was observed. However, for other catalysts, the value was greater than 5. In the tri-reforming process, the H_2/CO ratio is controlled by the following reactions:
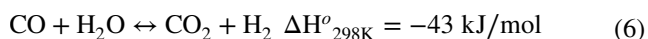
Dry reforming of methane (DRM):

$$CO_2 + CH_4 \leftrightarrow 2CO + 2H_2 \quad \Delta H^o_{298K} = +247.3 \text{ kJ/mol} \quad (3)$$

Steam reforming of methane (SRM):

$$CH_4 + H_2O \leftrightarrow CO + 3H_2 \quad \Delta H^o_{298K} = +206.3 \text{ kJ/mol} \quad (4)$$

Partial oxidation methane (POM):

$$CH_4 + {}^1\!/_2\, O_2 \leftrightarrow CO + 2H_2 \quad \Delta H^o_{298K} = -35.6 \text{ kJ/mol} \quad (5)$$

Water gas shift reaction (WGSR):

$$CO + H_2O \leftrightarrow CO_2 + H_2 \quad \Delta H^o_{298K} = -43 \text{ kJ/mol} \quad (6)$$
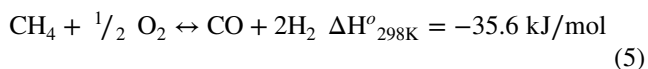
It was observed that, over NZ-250 catalyst, the obtained H_2/CO molar ratio was very high (∼8.0). With decreasing the Zr-content in the catalyst, the H_2/CO molar ratio decreased and reached 1.9 for NZ-1000. Furthermore, for NZ-1500 and NZ-2000 catalysts, the H_2/CO molar ratio again increased to ∼8.0. A very well correlation with the physicochemical properties of the catalyst was observed, as shown in Table 2. With decreasing the Zr-content in the catalyst from NZ-250 to NZ 2000, the BET surface area, total pore volume, and pore diameter of the final catalyst were increased, and the surface area (16.1 m²/g), total pore volume (0.063 cm³/g), pore diameter (18 nm) were highest for NZ-1000. On the other hand, the hydrogen consumption, reducibility of nickel metal, active nickel metal surface area, and metal dispersion passed through a maximum with decreasing the Zr-content in the catalyst. These values were also maximum for NZ-1000. In addition to that, the nickel crystallite size of the NZ-1000 catalyst was lowest (50 nm). This observed trend of the physicochemical properties of the final catalysts indicated that the variation of the ratio of Zr-precursor, ligand, and solvent played a significant role in controlling the final structural morphology as well as the physicochemical properties of the final catalyst.

For the NZ-1000 catalyst, the lowest H_2/CO ratio of 1.9 was observed because of the simultaneous occurrence of SRM, DRM, and POM, respectively. This is nothing but the tri-reforming of methane (TRM), and for TRM, the typical H_2/CO ratio is usually obtained as 1.5–2 (James et al. 2011; Sun et al. 2012). This result suggested that the TRM was highly favorable over NZ-1000 catalyst because of its desired physio-chemical properties, including the highest surface area (16 m²/g), nickel metal surface area (2.3 m². g$_{cat}^{-1}$), metal dispersion (7.1%), nickel metal reducibility (45%), and smallest nickel crystallite size (∼32 nm), respectively. For the other catalysts, the H_2/CO ratio was very high (> 5) because of less CO_2 conversion and more hydrogen formation due to WGSR.

The carbon deposition on the catalysts during the reaction was evaluated by characterizing the spent catalyst using CHNS analysis. As shown in Fig. 9b, the obtained carbon formation rate also followed a similar trend as observed for the H_2/CO ratio over all the catalysts. The carbon formation rate was the lowest (1.67 mmol. g$_{cat}^{-1}$. h^{-1}) for the NZ-1000 catalyst, which suggested that the side reactions related to coke formation were also minimal over the NZ-1000 catalyst compared to others. The observed carbon formation rate for the other catalyst was higher (2.83–5.33 mmol. g$_{cat}^{-1}$. h^{-1}) because of its bigger nickel particle size (> 50 nm). Bigger Ni particles facilitated the carbon formation via methane cracking ($CH_4 \leftrightarrow C + 2H_2$) in combination with the boudouard reaction ($2CO \leftrightarrow CO_2 + C$), respectively (Pino et al. 2011; Pham et al. 2021). In addition to that, carbon formation is also favored due to the presence of strong strength basic sites in the catalyst. The catalyst screening study suggested that the NZ-1000 catalyst was more suitable for tri-reforming reactions and that carbon deposition was also the lowest. Therefore, this catalyst was chosen for further reaction parameter study, the results are discussed in the following section.

Effect of temperature

The effect of temperature (600–850 °C) over NZ-1000 catalyst was evaluated at the standard reaction condition discussed in the previous section. The results are plotted in Fig. 10.

As shown in Fig. 10, the conversion of CO_2 was maximum (∼11%) at 700 °C. At low temperatures (< 700 °C), the CO_2 conversion was very low (1.9–3.4%) because of a higher rate of water gas shift reaction (WGSR) as compared to the reforming reaction (Walker et al. 2012). At 700–750 °C, the CO_2 conversion increased due to the favorable environment of endothermic SRM and DRM reactions, respectively (Sun et al. 2012; Singha et al. 2016a). For CH_4, a very high conversion of 63.1% was
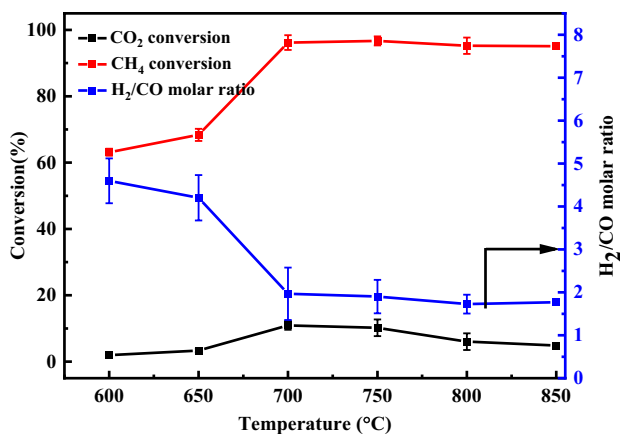
Fig. 10 Effect of temperature over NZ-1000 catalyst. Reaction condition: Feed ($CH_4/CO_2/O_2/H_2O/N_2$) ratio of (1/0.5/0.1/0.0125/1), 1 atm., and 1 g catalyst

achieved even at $600 - C$, reaching the maximum of ~ 97% at $\geq 700\ °C$. Very high CH_4 conversion was achieved due to dispersed small-sized nickel particles, which facilitated both SRM and DRM reactions that consumed CH_4 (Ryi et al. 2014; Anchieta et al. 2019). The presence of oxidants such as O_2 and H_2O also enhanced the methane conversion. In addition to that, at higher temperatures, easy decomposition of CH_4 in the presence of nickel metal also increases the CH_4 conversion (Lee et al. 2003).

At low temperatures ($\leq 650\ °C$), the H_2/CO molar ratio was high (4.6), and this value decreased with temperature and reached to 1.7 at $\geq 800\ °C$. The H_2/CO ratio was high at low temperatures because of more hydrogen formation via exothermic POM and WGS reactions, respectively. At low temperatures, the POM and WGS reactions were favored compared to the endothermic SRM and DRM reactions, which produced more CO (Majewski and Wood 2014; García-Vargas et al. 2015). H_2 and CO were produced via POM, while CO was simultaneously converted to CO_2 and H_2 via the WGS reaction, which resulted a higher hydrogen formation than CO and a high H_2/CO ratio. However, at $\geq 700\ °C$, DRM reaction activated along with POM and SRM reaction, which increased CO formation and reduced the H_2/CO ratio (Amin and Yaw 2007). The effect of the temperature study demonstrated that the H_2/CO ratio of ~ 1.9 could be achieved at a temperature of 700–750 °C in the presence of the NZ-1000 catalyst.

Time on stream study

In general, the synthesis gas with an H_2/CO mole ratio of ~ 1.5–2 is highly desirable as a feed for the Fischer–Tropsch process for the production of more valuable methanol, dimethyl ether (DME), higher alkenes,

etc. (Majewski and Wood 2014; Singha et al. 2016b). Therefore, the catalyst that produces the consistent H_2/CO ratio of ~ 1.5–2 via the TRM process has huge commercial potential. As discussed in the previous section, the NZ-1000 catalyst exhibited better activity as compared to other catalysts developed for the TRM process. In the presence of this catalyst, the obtained H_2/CO ratio was ~ 1.7–2, and the carbon formation rate was also very low. Therefore, to verify the stability and consistency of this catalyst, the time-on-stream analysis was performed at the optimum reaction condition identified. The results obtained are plotted in Fig. 11.

The results reported in Fig. 11 depicted that, at 750 °C, in the presence of NZ-1000 catalyst, the conversion of CH_4 (89–92%) and CO_2 (~ 10–11%) was very consistent for 12.5 h. The H_2/CO ratio was also within the range of 1.6–2 for 12 h. The consistent performance of the catalyst was obtained due to the high thermal stability of Ni/ZrO_2 catalyst derived from MOF, the strong metal support interaction, high degree of reducibility, and high metal dispersion over NZ-1000 catalyst (Pham et al. 2021; Gupta and Deo 2023). The constant H_2/CO molar ratio also dictated that the TRM reaction was stable. For this consistent performance of the catalyst, ZrO_2 played an important role because of its high ionic conductivity and capability for the mobility of oxygen ions (Wang et al. 2021; Kozonoe et al. 2023). In addition to that, the strong nickel metal and support interaction, nickel metal dispersion also played a vital role in long-term stability at 750 °C. It is very important to highlight that the NZ-1000 catalyst developed in this study was superior which produced the desired H_2/CO ratio of ~ 1.6–2 at a low reaction temperature of 750 °C as compared to the previously reported catalysts (Garcia-Vargas et al. 2015).
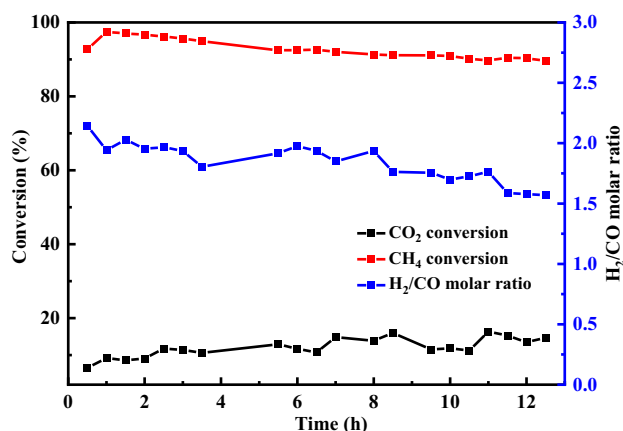

Fig. 11 Time-on-stream study over NZ-1000 catalyst at 750 °C. Reaction condition: Feed ($CH_4/CO_2/O_2/H_2O/N_2$) ratio of (1/0.5/0.1/0.0125/1), 1 atm., and 1 g catalyst

Comparison of TRM activity of Ni/ZrO₂ catalyst

In the previous literature, the Ni/ZrO$_2$ catalysts were mostly synthesized by precipitation and co-precipitation methods, followed by wet impregnation of nickel metal. The reported catalyst surface area was ≤ 17 m^2.g^{-1} (Table S2). However, Sun et al. (2012) obtained a slightly higher BET surface area of 27.8 m^2. g^{-1}, and Singha et al. (2016a) reported relatively high surface area of 128 m^2.g^{-1} for Ni/ZrO$_2$ catalyst synthesized by solvothermal and urea deposition–precipitation method. The typical reported pore diameter of the catalyst was ~ 5 nm, the reported nickel metal dispersion was very low (~ 2%), or most of the work was not reported.

The activity of various Ni/ZrO$_2$ catalysts was compared in Table S2. It has been observed from Table S2 that the reaction temperature was very high, > 800 °C, and in most of the studies, the information related to catalyst stability and carbon deposition is missing (Song and Pan 2004; Sun et al. 2012; Singha et al. 2016a). Kumar et al. (2019) reported a very low surface area (1 m^2. g^{-1}) and metal dispersion (2%). The carbon deposition rate was very high (23 mmol. g^{-1}.h^{-1}) at 800 °C. Anchieta et al. (2019) obtained approximately similar BET surface area (17 m^2. g^{-1}) and CO$_2$ conversion (~ 10%) with the present work. However, the CH$_4$ conversion was low (45%), and catalyst stability was shown for 5 h. In this study, the CH$_4$ conversion was very high (~96%) and the catalyst was stable for ~12 h.

CH$_4$ conversion (~ 96%) was obtained due to high metal dispersion (~ 7%), and the catalyst was stable > 12 h. The operating temperature (750 °C) was comparatively low, and the carbon deposition rate was also insignificant (1.67 mmol. g^{-1}.h^{-1}). Most importantly, the obtained H$_2$/CO ratio was consistent (1.5–2.0) for a longer period of time. The syn-gas with an H$_2$/CO ratio of 1.5–2 is essential as a feedstock for the Fischer–Tropsch process to produce higher alkenes, dimethyl ether (DME), methanol, etc. Therefore, comparatively, a better TRM activity was achieved with the Ni/ZrO$_2$ catalyst synthesized via the MOF route.

Conclusions

In this study, Zr-MOF were synthesized by varying the molar ratio of Zr precursor/BDC/DMF using a solvothermal method followed by calcination at different temperatures. Ni-metal was impregnated onto the Zr-MOF using the impregnation method and tested for TRM reaction. The catalyst characterization results revealed significant variations in the physicochemical properties of both the support (Zr-MOF) and the Ni/ZrO$_2$ catalysts derived from MOF. XRD analysis indicated that an appropriate ratio of metal precursors to solvent is crucial for achieving the desired MOF structure. XRD results also confirmed that the tetragonal structure of

Zr-MOF transformed into the monoclinic phase of ZrO$_2$ after calcination. After Ni-loading over Zr-MOF, notable variations were observed in terms of the reducibility of Ni metal, metal-support interaction, nickel crystallite size, active metal surface area, metal dispersion, and catalyst morphology as determined by TPR, XRD, chemisorption, HR-TEM, FE-SEM, respectively. The obtained BET surface area, total pore volume, average pore diameter, reducibility, and nickel metal dispersion were highest for the NZ-1000 catalyst.

The catalytic test demonstrated that the TRM reaction was highly favorable over NZ-1000 catalyst due to its desirable physicochemical properties, including the highest surface area (16 m^2/g), nickel metal surface area (2.3 m^2/g$_{cat}^{-1}$), metal dispersion (7.1%), nickel metal reducibility (45%), and smallest nickel crystallite size (~ 50 nm), respectively. For most catalysts, at lower temperatures (< 650 °C), CO$_2$ conversion was low because of a higher rate of WGSR. In comparison, CO$_2$ conversion increased at higher temperatures due to the SRM and DRM reactions, respectively. The effect of temperature data indicated that TRM was mostly favorable in the range of 700–800 °C. In the presence of the NZ-1000 catalyst, an optimum H$_2$/CO molar ratio of ~ 1.7–1.9 was achieved at temperatures of ≤ 700 °C with CH$_4$ and CO$_2$ conversions of ~ 96% and ~ 10%, respectively. However, for other catalysts, the H$_2$/CO molar ratio was very high (> 5) because of more WGS reaction than SRM and DRM reaction. Time-on-stream studies demonstrated that the NZ-1000 catalyst was thermally stable for ~ 12 h at 750 °C and maintained a consistent TRM activity with the H$_2$/CO ratio of 1.6–2. The better performance of the catalyst was attributed to the formation of the desired Zr-MOF structure, highest BET surface area, total pore volume, average pore diameter, reducibility, and nickel metal dispersion. The characterization results of the spent catalyst also supported its stability with a minimal amount of carbon deposition rate. Hence, the Ni/ZrO$_2$ catalyst derived from MOF was promising for the TRM process.

Data availability The data will be available on request.

Declarations

Ethics approval Not applicable.

Consent to participate All the authors contributed to complete this manuscript.

Consent for publication All of the authors agreed for the publication.

Competing interests The authors declare no competing interests.

References

Al-Fatesh A, Singh SK, Kanade GS et al (2018) Rh promoted and ZrO_2/Al_2O_3 supported Ni/Co based catalysts: high activity for CO_2 reforming, steam–CO_2 reforming and oxy–CO_2 reforming of CH_4. Int J Hydrogen Energy 43:12069–12080. https://doi.org/10.1016/j.ijhydene.2018.04.152

Alli RD, de Souza PAL, Mohamedali M et al (2023) Tri-reforming of methane for syn-gas production using Ni catalysts: current status and future outlook. Catal Today 407:107–124. https://doi.org/10.1016/j.cattod.2022.02.006

Amin NAS, Yaw TC (2007) Thermodynamic equilibrium analysis of combined carbon dioxide reforming with partial oxidation of methane to syn-gas. Int J Hydrogen Energy 32:1789–1798. https://doi.org/10.1016/j.ijhydene.2006.12.004

Anchieta CG, Assaf EM, Assaf JM (2019) Effect of ionic liquid in Ni/ZrO_2 catalysts applied to syn-gas production by methane tri-reforming. Int J Hydrogen Energy 44:9316–9327. https://doi.org/10.1016/j.ijhydene.2019.02.122

Ardila-Suárez C, Rodríguez-Pereira J, Baldovino-Medrano VG, Ramírez-Caballero GE (2019) An analysis of the effect of zirconium precursors of MOF-808 on its thermal stability, and structural and surface properties. Cryst Eng Comm 21:1407–1415. https://doi.org/10.1039/c8ce01722k

Bai Y, Dou Y, Xie LH et al (2016) Zr-based metal-organic frameworks: design, synthesis, structure, and applications. Chem Soc Rev 45:2327–2367

Biswas P, Kunzru D (2007) Steam reforming of ethanol for production of hydrogen over $Ni/CeO2-ZrO2$ catalyst: effect of support and metal loading. Int J Hydrogen Energy 32:969–980. https://doi.org/10.1016/j.ijhydene.2006.09.031

Cavka JH, Jakobsen S, Olsbye U et al (2008) A new zirconium inorganic building brick forming metal organic frameworks with exceptional stability. J Am Chem Soc 130:13850–13851. https://doi.org/10.1021/ja8057953

Chein RY, Hsu WH (2018) Thermodynamic analysis of syn-gas production via tri-reforming of methane and carbon gasification using flue gas from coal-fired power plants. J Clean Prod 200:242–258. https://doi.org/10.1016/J.JCLEPRO.2018.07.228

Fiaschi D, Baldini A (2009) Joining semi-closed gas turbine cycle and tri-reforming: SCGT-TRIREF as a proposal for low CO_2 emissions powerplants. Energy Convers Manag 50:2083–2097. https://doi.org/10.1016/j.enconman.2009.03.034

Finsel M, Hemme M, Döring S et al (2019) Synthesis and thermal stability of $ZrO_2@SiO_2$ core-shell submicron particles. RSC Adv 9:26902–26914. https://doi.org/10.1039/c9ra05078g

Furukawa H, Gándara F, Zhang YB et al (2014) Water adsorption in porous metal-organic frameworks and related materials. J Am Chem Soc 136:4369–4381. https://doi.org/10.1021/ja500330a

García-Vargas JM, Valverde JL, Díez J et al (2015) Catalytic and kinetic analysis of the methane tri-reforming over a Ni-Mg/β-SiC catalyst. Int J Hydrogen Energy 40:8677–8687. https://doi.org/10.1016/j.ijhydene.2015.05.032

Gupta S, Deo G (2023) Effect of metal amount on the catalytic performance of Ni–Al_2O_3 catalyst for the tri-reforming of methane. Int J Hydrogen Energy 48:5478–5492. https://doi.org/10.1016/j.ijhydene.2022.11.049

Halmann M, Steinfeld A (2006) Thermoneutral tri-reforming of flue gases from coal- and gas-fired power stations. Catal Today 115:170–178. https://doi.org/10.1016/j.cattod.2006.02.064

Horti NC, Kamatagi MD, Nataraj SK, et al (2020) Structural and optical properties of zirconium oxide ($ZrO2$) nanoparticles: effect of calcination temperature. Nano Express 1. https://doi.org/10.1088/2632-959X/ab8684

James OO, Maity S, Mesubi MA et al (2011) Towards reforming technologies for production of hydrogen exclusively from renewable resources. Green Chem 13:2272–2284. https://doi.org/10.1039/c0gc00924e

Jiang H, Li H, Fan H (2013) Tri-reforming of methane over Pt modified Ni/MgO catalysts under atmospheric pressure-thermal distribution in the catalyst bed. In: Appl Mech Mater 255–258

Jiang H, Li H, Xu H, Zhang Y (2007) Preparation of $Ni/Mg_xTi_{1-x}O$ catalysts and investigation on their stability in tri-reforming of methane. Fuel Process Technol 88:988–995. https://doi.org/10.1016/j.fuproc.2007.05.007

Kozonoe CE, de Abreu TF, de Brito Alves RM, Schmal M (2023) Influence of the material as support for nickel on the product selectivity of the tri-reforming of methane. Mater Today Commun 35. https://doi.org/10.1016/j.mtcomm.2023.105732

Kumar A, Vikrant K, Younis SA, Kim KH (2023) Tuning of active nickel species in MOF-derived nickel catalysts for the control on acetic acid steam reforming and hydrogen production. Int J Hydrogen Energy 48:14964–14977. https://doi.org/10.1016/j.ijhydene.2023.01.036

Kumar KDPL, Naidu BN, Sarkar B, et al (2021) Enhanced CO_2 utilization via methane tri-reforming over Ru incorporated Co/MgO-Al_2O_3 catalyst: influence of La and Ce promoters. J Environ Chem Eng 9. https://doi.org/10.1016/j.jece.2021.105949

Kumar R, Kumar K, Choudary NV, Pant KK (2019) Effect of support materials on the performance of Ni-based catalysts in tri-reforming of methane. Fuel Process Technol 186:40–52. https://doi.org/10.1016/j.fuproc.2018.12.018

Kumar R, Pant KK (2020) Promotional effects of Cu and Zn in hydrotalcite-derived methane tri-reforming catalyst. Appl Surf Sci 515. https://doi.org/10.1016/j.apsusc.2020.146010

Lan X, K.W. Thoning, E.J. Dlugokencky (2024) Trends in globally averaged CH_4, N_2O, and SF_6 determined from NOAA Global Monitoring Laboratory measurements. version 2024: https://doi.org/10.15138/P8XG-AA10

Lee HY, Kim AR, Park M-J et al (2015) Combined steam and CO_2 reforming of CH_4 using coke oven gas on nickel-based catalyst: effects of organic acids to nickel dispersion and activity. Chem Eng J 280:771–781. https://doi.org/10.1016/j.cej.2015.06.047

Lee SH, Cho W, Ju WS et al (2003) Tri-reforming of CH_4 using CO_2 for production of synthesis gas to dimethyl ether. In: Catalysis Today. pp 133–137

Li D, Xu HQ, Jiao L, Jiang HL (2019) Metal-organic frameworks for catalysis: state of the art, challenges, and opportunities. Energy Chem 1:100005. https://doi.org/10.1016/J.ENCHEM.2019.100005

Liu N, Shi L, Meng X (2019) Tuning the adsorption properties of UiO-66 via acetic acid modulation. J Chem Sci 131. https://doi.org/10.1007/s12039-019-1628-3

Majewski AJ, Wood J (2014) Tri-reforming of methane over Ni@SiO_2 catalyst. Int J Hydrogen Energy 39:12578–12585. https://doi.org/10.1016/j.ijhydene.2014.06.071

Pan W, Zheng J, Song C (2002) Catalytic tri-reforming of methane using flue gas from fossil fuel-based power plants. Fuel Chem Div 47:262–264

Pandey A, Biswas P, Pant KK, Dalai AK (2024) Tri-reforming of CH_4 over a thermally stable and carbon-resistant nanonickel metal catalyst dispersed on mesoporous-zirconia. Ind Eng Chem Res 63:1000–1012. https://doi.org/10.1021/acs.iecr.3c03645

Pham Minh D, Pham XH, Siang TJ, N. Vo DV (2021) Review on the catalytic tri-reforming of methane - part I: impact of operating conditions, catalyst deactivation and regeneration. Appl Catal A Gen 621. https://doi.org/10.1016/j.apcata.2021.118202

Pham XH, Ashik UPM, Hayashi JI, et al (2021) Review on the catalytic tri-reforming of methane - part II: catalyst development. Appl Catal A Gen 623. https://doi.org/10.1016/j.apcata.2021.118286

Pino L, Vita A, Cipitì F et al (2011) Hydrogen production by methane tri-reforming process over Ni-ceria catalysts: effect of La-doping. Appl Catal B 104:64–73. https://doi.org/10.1016/j.apcatb.2011.02.027

Ragon F, Horcajada P, Chevreau H et al (2014) In situ energy-dispersive X-ray diffraction for the synthesis optimization and scale-up of the porous zirconium terephthalate UiO-66. Inorg Chem 53:2491–2500. https://doi.org/10.1021/ic402514n

Ryi S-K, Lee S-W, Park J-W et al (2014) Combined steam and CO_2 reforming of methane using catalytic nickel membrane for gas to liquid (GTL) process. Catal Today 236:49–56. https://doi.org/10.1016/j.cattod.2013.11.001

Sai T, Ran S, Guo Z, et al (2020) Deposition growth of Zr-based MOFs on cerium phenyl phosphonate lamella towards enhanced thermal stability and fire safety of polycarbonate. Compos B Eng 197. https://doi.org/10.1016/j.compositesb.2020.108064

Schmal M, Toniolo FS, Kozonoe CE (2018) Perspective of catalysts for (Tri) reforming of natural gas and flue gas rich in CO_2. Appl Catal A Gen 568:23–42. https://doi.org/10.1016/j.apcata.2018.09.017

Seetharaj R, Vandana PV, Arya P, Mathew S (2019) Dependence of solvents, pH, molar ratio and temperature in tuning metal organic framework architecture. Arab J Chem 12:295–315

Singha RK, Das S, Pandey M et al (2016a) Ni nanocluster on modified CeO_2-ZrO_2 nanoporous composite for tri-reforming of methane. Catal Sci Technol 6:7122–7136. https://doi.org/10.1039/c5cy01323b

Singha RK, Shukla A, Yadav A et al (2016b) Energy efficient methane tri-reforming for synthesis gas production over highly coke resistant nanocrystalline Ni-ZrO_2 catalyst. Appl Energy 178:110–125. https://doi.org/10.1016/j.apenergy.2016.06.043

Solov'ev SA, Gubareni YV, Kurilets YP et al (2012) Tri-reforming of methane on structured Ni-containing catalysts. Theor Exp Chem 48:199–205. https://doi.org/10.1007/s11237-012-9262-x

Song C (2001) Tri-reforming: Anew process for reducing CO_2 emission. In: Chemical Innovation. pp 21–26.

Song C, Pan W (2004) Tri-reforming of methane: a novel concept for catalytic production of industrially useful synthesis gas with desired H_2/CO ratios. In: Catalysis Today. pp 463–484.

Sun LZ, Tan YS, De ZQ et al (2012) Tri-reforming of coal bed methane to syn-gas over the Ni-Mg-ZrO_2 catalyst. J Fuel Chem Technol 40:831–837. https://doi.org/10.1016/s1872-5813(12)60032-2

Tu J-Y, Shen C-H, Tsai D-H, Kung C-W (2023) Carbonized nickel-incorporated metal–organic frameworks for methane reforming: post-synthetic modification vs impregnation. ACS Appl Nano Mater 6:10269–10279. https://doi.org/10.1021/acsanm.3c01173

Walker DM, Pettit SL, Wolan JT, Kuhn JN (2012) Synthesis gas production to desired hydrogen to carbon monoxide ratios by tri-reforming of methane using Ni-MgO-(Ce, Zr)$_O$2 catalysts. Appl Catal A Gen 445–446:61–68. https://doi.org/10.1016/j.apcata.2012.08.015

Wang X, Bai X, Guo Y et al (2021) A nanoscale Ni/ZrO_2 catalyst coated with Al_2O_3 for carbon dioxide reforming of methane. J Chem Technol Biotechnol 96:474–480. https://doi.org/10.1002/jctb.6562

Wen J, Zhu T, Xie Z et al (2017) A strategy to obtain a high-density and high-strength zirconia ceramic via ceramic injection molding by the modification of oleic acid. Int J Miner Metall Mater 24:718–725. https://doi.org/10.1007/s12613-017-1455-9

Yoo J, Bang Y, Han SJ et al (2015) Hydrogen production by tri-reforming of methane over nickel-alumina aerogel catalyst. J Mol Catal A Chem 410:74–80. https://doi.org/10.1016/j.molcata.2015.09.008

Zhang Y, Zhang S, L. Gossage J, et al (2014) Thermodynamic analyses of tri-reforming reactions to produce syn-gas. Energy Fuels 28:2717–2726. https://doi.org/10.1021/ef500084m

Zhao ZW, Zhou X, Liu YN et al (2018) Ultrasmall Ni nanoparticles embedded in Zr-based MOFs provide high selectivity for CO_2 hydrogenation to methane at low temperatures. Catal Sci Technol 8:3160–3165. https://doi.org/10.1039/c8cy00468d

Zhen W, Li B, Lu G, Ma J (2015) Enhancing catalytic activity and stability for CO_2 methanation on Ni@MOF-5 via control of active species dispersion. Chem Commun 51:1728–1731. https://doi.org/10.1039/c4cc08733j